Realizing Constant Current and Constant Voltage Outputs and Input Zero Phase Angle of Wireless Power Transfer Systems With Minimum Component Counts

Jianghua Lu, *Student Member, IEEE*, Guorong Zhu, *Senior Member, IEEE*, Deyan Lin, *Member, IEEE*, Yiming Zhang, *Member, IEEE*, Haoran Wang, *Member, IEEE*, and Chunting Chris Mi, *Fellow, IEEE*

***Abstract*— In both normal and fast wireless electric vehicle charging systems, constant current/constant voltage (CC/CV) charging profile, regardless of the variation of the battery state of charge, is one of the most essential characteristics to ensure the battery performance and reliability. The input zero phase angle (ZPA) is able to minimize the system volt-ampere rating, enhance the power transfer capability, and make it easy to achieve soft-switching operation over the full range of battery charging profile. Therefore, the load-independent CC and CV output characteristics with ZPA conditions are necessary for wireless charging systems. However, the existing methods that can achieve these functions either add power switches or need a large number of compensation components, which make the system inefficient, uneconomical, and bulky. In this paper, a unified resonant tuning configuration with minimum passive component counts is proposed to achieve CC and CV outputs at two ZPA operating frequencies. According to the proposed configuration, all the possible inductive power transfer (IPT) and capacitive power transfer (CPT) topologies are analogized. With these topologies, both CC and CV outputs with ZPA are achieved using a minimum number of compensation components and no additional power switches. Among all the simplest IPT topologies, a primary Series-secondary Series and Parallel (S-SP) compensation topology is illustrated to demonstrate the analysis.**

***Index Terms*— Capacitive power transfer (CPT), constant current (CC), constant voltage (CV), inductive power transfer (IPT), zero phase angle (ZPA), zero voltage switching (ZVS).**

I. Introduction

Li-ION battery is expected to grow fast in various energy storage applications such as, but not limited to, implantable pacemaker, cell phones, laptops, automated guided vehicles (AGVs) and electric vehicles (EVs) due to the advantages of its high specific energy, energy density, and high cycle lifetime. The wireless power transfer (WPT) technology [1], [2] using magnetic or electric field coupling, namely the inductive power transfer (IPT) or capacitive power transfer (CPT), provides a promising solution for both normal and fast charging [3], [4] of EV Li-ion batteries. Over the full range of the Li-on battery charge, the battery pack equivalent load resistance, which defined as the ratio of the charging voltage to the charging current, may be roughly from a few ohms to several hundred ohms [5]. With such a wide load range, a load-independent constant current/constant voltage (CC/CV) charging profile [5]–[9] is desirable to ensure safety, durability, and performance of the battery. On the other hand, the zero phase angle (ZPA) between the input voltage and current, namely unit power factor, can minimize the apparent power required and enhance the power transfer capability [8]–[11]. Furthermore, based on ZPA, a zero voltage switching (ZVS) condition for the primary MOSFET-based inverter can be easily achieved to improve the system efficiency by slightly changing the value of a compensation component [9], [12], [13] or the operating frequency [8], [14], or utilizing phase-shift control [15]. So, both CC and CV output characteristics with input ZPA are necessary for wireless battery charging systems.

A front- or back-end DC/DC converter is usually used to realize CC and CV output characteristics in WPT systems [11], [16], meanwhile, a variable frequency control method is applied to achieve ZPA [17]. However, the additional DC/DC converter will undoubtedly increase the system cost and decrease the power density and the efficiency of the system. In addition, instability issue is inevitable for the variable frequency control [18]. In order to avoid the above drawbacks, designing specified resonant conditions for the resonant compensation topology in the WPT system are currently effective solutions to achieve CC and/or CV outputs with ZPA conditions. The load-independent output and/or input characteristics of some widely-used compensation topologies in both IPT and CPT systems are summarized in Tab. I [12]–[14], [19]–[38]. From Tab. I, one can conclude that

1) Among all these compensation topologies, only the double-sided LCC topology in the IPT system has been designed to achieve CC and CV outputs at two different ZPA frequencies [8], [9].

Manuscript received August 6, 2019; revised December 15, 2019 and February 19, 2020; accepted March 23, 2020. Date of publication April 16, 2020; date of current version December 24, 2020. This work was supported in part by the Scholarship from the China Scholarship Council and in part by the National Natural Science Foundation of China under Grant 51777146 and Grant 51977163. The Associate Editor for this article was Z. Li. *(Corresponding author: Chunting Chris Mi.)*

Jianghua Lu, Guorong Zhu, and Deyan Lin are with the School of Automation, Wuhan University of Technology, Wuhan 430070, China (e-mail: tri_ljh@whut.edu.cn; zhgr_55@whut.edu.cn; deyanlin@whut.edu.cn).

Yiming Zhang and Chunting Chris Mi are with the Department of Electrical and Computer Engineering, San Diego State University, San Diego, CA 92182 USA (e-mail: zhangym07@gmail.com; cmi@sdsu.edu).

Haoran Wang is with the Department of Energy Technology, Aalborg University, 9220 Aalborg, Denmark (e-mail: hao@et.aau.dk).

Digital Object Identifier 10.1109/TITS.2020.2985658

TABLE I
LITERATURE REVIEW ON COMPENSATION TOPOLOGIES AND THEIR LOAD-INDEPENDENT OUTPUT AND/OR INPUT CHARACTERISTICS

Systems	Topologies	CC mode	CV mode	ZPA in CC mode	ZPA in CV mode
IPT	S-S	[14], [19]–[27]	[14], [23], [24], [27]–[29]	[19]–[26]	No
	S-P	[14], [19], [21]	[14], [21], [28], [30]	Not yet	[21], [30]
	P-S	No	[14], [21]	No	[21]
	P-P	[14], [21]	No	[21]	No
	S-SP	[27]	[23], [27], [30]–[33]	Not yet	[23], [30]–[33]
	S-CLC	[34]	Not yet	[34]	Not yet
	S-LCC	Not yet	[13]	Not yet	[13]
	LCC-S	[27]	[11], [23], [27], [30]	Not yet	[11], [30]
	LCC-P	[22], [23], [25]	Not yet	[22], [25]	Not yet
	Double-sided LCL	[25], [35]	Not yet	[25], [35]	Not yet
	Double-sided LCC	[8], [9], [12], [23], [27]	[8], [9], [27], [30]	[8], [9], [12]	[8], [9], [30]
CPT	Double-sided LCL	[36]	Not yet	[36]	Not yet
	CLC(Π)-CLC(T)	[37]	[37]	[37]	Not yet
	Double-sided LC	[38]	[38]	Not yet	Not yet

2) Hybrid topologies [21], [39], [40] that combine different compensation topologies, for example, combining S-S and P-S [21], can achieve CC/CV charging with ZPA conditions.

However, the exiting efforts still have the following challenges:

1) In the hybrid compensation topologies, additional power semiconductor devices are needed, which increase the system cost and power loss, and decrease the system reliability.
2) Although there is no need for additional power semiconductor devices for the double-sided LCC topology, the six additional compensation components in the double-sided LCC compensation topology, especially the primary and secondary compensation inductors, result in a large system volume, weight, and cost and will limit its applications where space and weight are constrained.
3) There is currently no literature on CC and CV outputs with ZPA conditions for CPT topology. So, if the CPT system is expected to be applied to charge Li-on batteries, more research about its load-independent output and input characteristics are necessary.

To address the aforementioned issues, we study the simplest topologies in IPT and CPT systems that can achieve both CC and CV outputs with ZPA using the least number of components. Specifically,

1) A fact is revealed that a resonant tuning configuration that just consists of four lumped passive components is the simplest resonant tank circuit to achieve CC and CV outputs with ZPA. It means that an arbitrary resonant tank circuit composed of four or more lumped components can be designed to realize CC and CV outputs at two different ZPA frequencies.
2) According to the proposed simplest resonant tank circuit, all the possible IPT and CPT topologies are analogized, which implies that as few compensation components as possible are needed in IPT and CPT systems to achieve CC and CV outputs with ZPA. Compared with hybrid topologies, there is no need of some bidirectional power switches for these topologies. Besides, it can improve volumetric and gravimetric power densities and decrease the cost of the system because fewer compensation components are needed compared with the double-sided LCC topology.
3) Among all the simplest IPT systems, an S-SP topology is chosen as an example to demonstrate the feasibility and validity of the analysis.

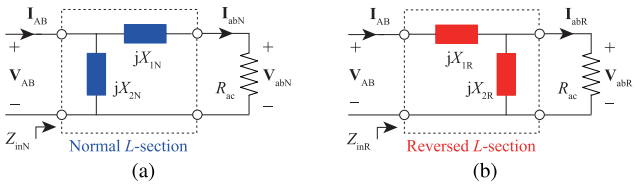

Fig. 1. (a) A normal L-section matching network and (b) a reversed L-section matching network.

II. NORMAL AND REVERSED L-SECTION MATCHING NETWORKS

The normal and reversed L-section matching networks, shown in Fig. 1(a) and 1(b) respectively, consisting of only two lumped components: a parallel reactance and a series reactance, are the two types of the most basic resonant circuit [41], [42]. In Fig. 1(a) and 1(b), X_{1N} and X_{2N} are the reactances of the normal L-section, X_{1R} and X_{2R} are the reactances of the reversed L-section, and R_{ac} represents an ac load resistance. The output voltage of the normal L-section ($\mathbf{V}_{abN}$) and the output current of the reversed L-section ($\mathbf{I}_{abR}$) are expressed as

$$\mathbf{V}_{abN} = \frac{R_{ac} \cdot jX_{2N}}{R_{ac} + (jX_{1N} + jX_{2N})}\mathbf{I}_{AB} \tag{1a}$$

$$\mathbf{I}_{abR} = \frac{jX_{2R}}{R_{ac} \cdot (jX_{1R} + jX_{2R}) + jX_{1R} \cdot jX_{2R}}\mathbf{V}_{AB} \tag{1b}$$

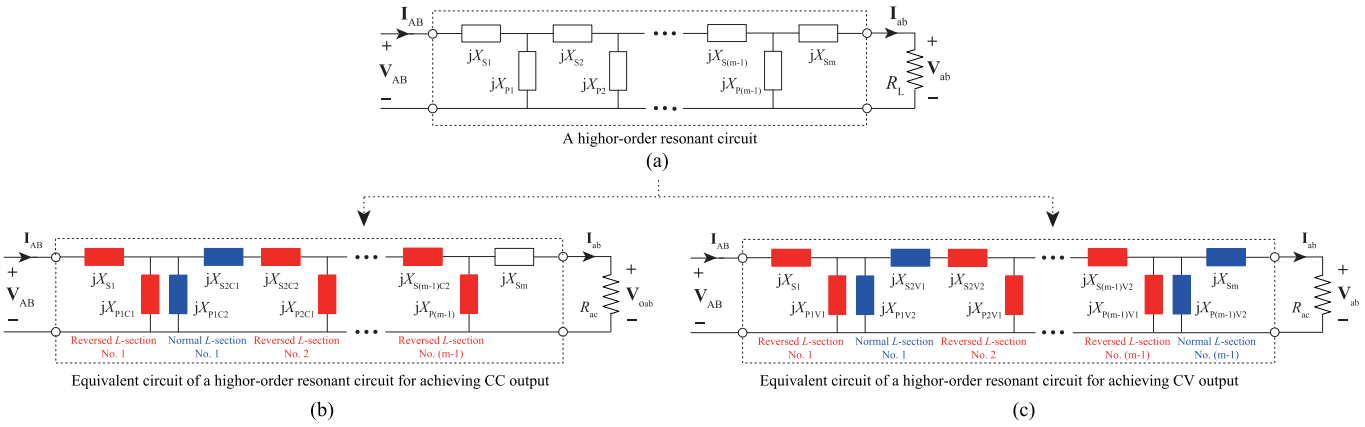

Fig. 2. A method of analyzing the load-independent output characteristics of an arbitrary resonant tank circuit. (a) A higher-order resonant circuit, (b) the equivalent circuit of Fig. 2(a) in CC mode, and (c) the equivalent circuit of Fig. 2(a) in CV mode.

where, $\mathbf{I}_{AB}$ and $\mathbf{V}_{AB}$ are the phasor forms of the input current and voltage.

In (1a) and (1b), $\mathbf{V}_{abN}$ and $\mathbf{I}_{abR}$ are independent of R_{ac} when $X_{1N} + X_{2N} = 0$ and $X_{1R} + X_{2R} = 0$ respectively, which are simplified as

$$\mathbf{V}_{abN} = \mathrm{j}X_{2N}\mathbf{I}_{AB} \tag{2a}$$

$$\mathbf{I}_{abR} = \frac{1}{\mathrm{j}X_{1R}}\mathbf{V}_{AB} \tag{2b}$$

The input impedances of the normal and reversed L-section matching networks are, respectively, given by

$$Z_{inN} = \frac{(R_{ac} + \mathrm{j}X_{1N})\,\mathrm{j}X_{2N}}{(R_{ac} + \mathrm{j}X_{1N}) + \mathrm{j}X_{2N}} = \frac{(R_{ac} + \mathrm{j}X_{1N})\,\mathrm{j}X_{2N}}{R_{ac} + (\mathrm{j}X_{1N} + \mathrm{j}X_{2N})} \tag{3a}$$

$$Z_{inR} = \frac{R_{ac}\cdot \mathrm{j}X_{2R}}{R_{ac} + \mathrm{j}X_{2R}} + \mathrm{j}X_{1R} = \frac{R_{ac}\,(\mathrm{j}X_{1R} + \mathrm{j}X_{2R}) - X_{1R}X_{2R}}{R_{ac} + \mathrm{j}X_{2R}} \tag{3b}$$

Under the conditions of $X_{1N}+X_{2N} = 0$ and $X_{1R}+X_{2R} = 0$, respectively, Z_{inN} and Z_{inR} are derived as

$$Z_{inN} = \frac{(R_{ac} + \mathrm{j}X_{1N})\,\mathrm{j}X_{2N}}{R_{ac}} \tag{4a}$$

$$Z_{inR} = \frac{-X_{1R}X_{2R}}{R_{ac} + \mathrm{j}X_{2R}} \tag{4b}$$

As aforementioned, a voltage-fed reversed L-section matching network has the output characteristic of a current source. The normal L-section driven by a current source can achieve CV output. Following this logic, a higher-order resonant circuit can be divided into cascaded connections of multiple normal and reversed L-section matching networks to simplify the analysis of its CC and CV output characteristics. The analysis method is shown in Fig. 2. Compared with this method, the conventional LC resonance model, namely Thevenin-Norton equivalencies, just can be applied to analyze CC or CV output of a resonant circuit. In the following sections, the method shown in Fig. 2 is adopted to discover the simplest resonant circuit that can achieve both CC and CV outputs at two ZPA operating frequencies.

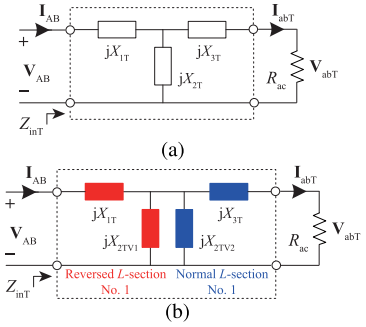

Fig. 3. (a) A T-circuit and (b) the equivalent circuit of the T-circuit in CV output.

III. Load-Independent CC and CV Outputs With ZPA Conditions

A. T- and π-Circuits

A T- or π-circuit is composed when a reactance is added in the normal or reversed L-section matching network. Fig. 3(a) shows a voltage-fed T-circuit, where, X_{1T}, X_{2T}, and X_{3T} are the passive components, and $\mathbf{V}_{abT}$ and $\mathbf{I}_{abT}$ are the phasor forms of the output voltage and current respectively.

According to Fig. 2, the T-circuit can be described as a series connected matching network of a reversed L-section (consisting of X_{1T} and X_{2T}) and the series reactance X_{3T}. According to the analysis of the previous section, the reversed L-section matching network can achieve CC output. And, X_{3T} does not affect the output current. So, CC output characteristic of the T-circuit can be obtained when $X_{1T} + X_{2T} = 0$. And the load-independent output current is expressed as

$$\mathbf{I}_{abT} = \frac{1}{\mathrm{j}X_{1T}}\mathbf{V}_{AB}\ \left(\text{or } \mathbf{G}_{TCC} = \frac{\mathbf{I}_{abT}}{\mathbf{V}_{AB}} = \frac{1}{\mathrm{j}X_{1T}}\right) \tag{5}$$

where, $\mathbf{G}_{TCC}$ represents the transconductance of the T-circuit.

With the condition of $X_{1T} + X_{2T} = 0$, the input impedance of the T-circuit (Z_{inT}) is derived as

$$Z_{inT} = \frac{-X_{1T}\cdot X_{2T}}{R_{ac} + \mathrm{j}X_{2T} + \mathrm{j}X_{3T}} \tag{6}$$

From (6), Z_{inT} is purely resistive and independent of R_{ac} when $X_{2T} + X_{3T} = 0$. It means that the load-independent

TABLE II

ANALYSIS OF THE LOAD-INDEPENDENT OUTPUT AND INPUT CHARACTERISTICS OF THE π-CIUCUIT

A current-fed π-circuit	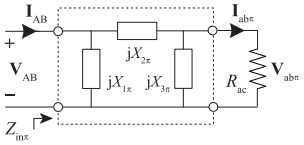	
Equivalent circuits	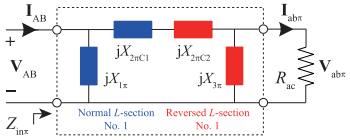 For achieving constant current output	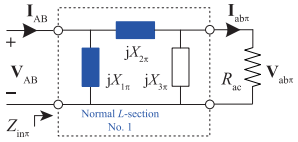 For achieving constant voltage output
Equivalent variables	$X_{2\pi} = X_{2\pi C1} + X_{2\pi C2}$	No
Conditions for achieving load-independent output	$X_{1\pi} + X_{2\pi C1} = X_{2\pi C2} + X_{3\pi C1} = 0$	$X_{1\pi} + X_{2\pi} = 0$
Mathematical models of load-independent outputs	$\mathbf{I}_{ab\pi} = (X_{1\pi}/X_{2\pi C2})\,\mathbf{I}_{AB}$	$\mathbf{V}_{ab\pi} = \mathrm{j}X_{1\pi}\mathbf{I}_{AB}$
Conditions for achieving load-independent ZPA	No	$\begin{cases} X_{1\pi} + X_{2\pi} = 0 \\ X_{2\pi} + X_{3\pi} = 0 \end{cases}$
Input impedance	No	$Z_{in\pi} = 1/(R_L X_{1\pi} X_{2\pi}) = 1/\left(R_{ac}\left\|\mathbf{G}^2_{\pi CV}\right\|\right)$

ZPA condition is achieved. And the purely resistive input impedance Z_{inT} is given by

$$Z_{inT} = \frac{-X_{1T}\cdot X_{2T}}{R_{ac}} = \frac{X_{1T}\cdot X_{1T}}{R_{ac}} = \frac{1}{R_{ac}}\left|\frac{\mathbf{V}_{AB}}{\mathbf{I}_{abT}}\right|^2 = \frac{1}{R_{ac}\left|\mathbf{G}_{TCC}\right|^2} \tag{7}$$

To analyze the load-independent voltage output characteristic of the T-circuit, it is considered as a back-to-back connected circuit of a reversed and a normal L-section matching networks according to Fig. 2, which is shown in Fig. 3(b). In such case, X_{2T} is split into two reactances X_{2TV1} and X_{2TV2} in parallel [$X_{2T} = (X_{2TV1}X_{2TV2})/(X_{2TV1} + X_{2TV2})$, here $X_{2TV1} + X_{2TV2} \neq 0$]. Then, according to the analysis of the reversed and normal L-section matching networks, CV output characteristic for Fig. 3(b) can be achieved when $X_{1T} + X_{2TV1} = X_{2TV2} + X_{3T} = 0$. And the constant output voltage $\mathbf{V}_{abT}$ is given by

$$\mathbf{V}_{abT} = \frac{\mathrm{j}X_{2TV2}}{\mathrm{j}X_{1T}}\mathbf{V}_{AB}\ \left(\text{or } \mathbf{G}_{TCV} = \frac{\mathbf{V}_{abT}}{\mathbf{V}_{AB}} = \frac{X_{2TV2}}{X_{1T}}\right) \tag{8}$$

where, $\mathbf{G}_{TCV}$ represents the voltage transfer ratio of the T-circuit.

Under the condition of $X_{1T} + X_{2TV1} = X_{2TV2} + X_{3T} = 0$, the input impedance is derived as

$$Z_{inT} = \frac{-R_{ac}X_{1T}X_{2TV1}}{R_{ac}\left(\mathrm{j}X_{2TV1} + \mathrm{j}X_{2TV2}\right) - X_{2TV2}X_{3T}} \tag{9}$$

In (9), there does not exist a resonant condition to make Z_{inT} purely resistive because $X_{2TV1} + X_{2TV2} \neq 0$. It means that the T-circuit cannot achieve ZPA input in CV mode.

From the analysis above, one can make a conclusion that CC and CV outputs can be achieved for the T-circuit. However, the load-independent ZPA condition is only achieved in CC mode. In IPT systems, the S-S topology is essentially a T-circuit [22], [23], [30]. According to the analysis of the T-circuit, therefore, the S-S can achieve CC output at a ZPA frequency, but CV mode operates at non-ZPA frequency. These results are in compliance with the analysis in [23], [24].

The analysis of the π-circuit is similar to that of the T-circuit and shown in Tab. II in detail. The π-circuit can be described as a back-to-back connected circuit of a normal and a reversed L-section matching networks, as shown in the second row and the second column of Tab. II. Also, according to the analysis of the L-section matching networks, the π-circuit can achieve CC output. However, there does not exist a resonant condition for the π-circuit to obtain the load-independent ZPA in CC mode.

The CV output characteristic and the input impedance in CV mode of the π-circuit are analyzed in the last column of Tab. II. The π-circuit is treated as series connection of a normal L-section and the parallel reactance $X_{3\pi}$. It can be seen that the load-independent output voltage and the ZPA condition are realized for the π-circuit.

So, for the T- and π-circuits, both CC and CV outputs can be realized. However, ZPA operating condition is only achieved for the T-circuit in CC mode or the π-circuit in CV mode. It means that the T- and π-circuits are not the simplest resonant tuning configuration to achieve CC and CV outputs both with ZPA conditions.

B. The Simplest Resonant Tuning Configuration

Based on the T- or π-circuit, a lumped component is added. Then an equivalent circuit shown in Fig. 4(a) is obtained. X_1, X_2, X_3, and X_4 represent the reactances.

According to Fig. 2, Fig. 4(a) is equivalent to Fig. 4(b) to analyze its CC output characteristic and input ZPA condition. Fig. 4(b) is actually a series connected circuit of two-stage reversed L-section matching networks and a normal L-section matching network. The corresponding equivalent variables are

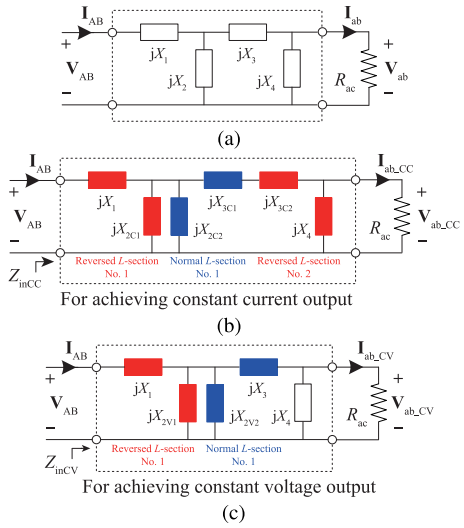

Fig. 4. (a) The simplest resonant tuning configuration that can be designed to achieve both CC and CV outputs with ZPA conditions, (b) the equivalent circuit of (a) to achieve CC output with ZPA, and (c) the equivalent circuit of (a) to achieve CV output with ZPA.

derived as

$$X_2 = \frac{X_{2C1}X_{2C2}}{X_{2C1}+X_{2C2}} \quad \text{and} \quad X_3 = X_{3C1}+X_{3C2} \tag{10}$$

According to the analysis of the reversed and normal L-section matching networks, when the equivalent variables in Fig. 4(b) satisfy the following resonant conditions:

$$X_1 + X_{2C1} = X_{2C2} + X_{3C1} = X_{3C2} + X_4 = 0 \tag{11}$$

the load-independent output current $\mathbf{I}_{ab\_CC}$ (or transconductance $\mathbf{G}_{CC}$) can be achieved, which is derived as

$$\mathbf{I}_{ab\_CC} = \frac{1}{\mathrm{j}X_1}\mathrm{j}X_{2C2}\frac{1}{\mathrm{j}X_{3C2}}\mathbf{V}_{AB} \ (\text{or } \mathbf{G}_{CC} = \frac{\mathbf{I}_{ab\_CC}}{\mathbf{V}_{AB}} = -\frac{\mathrm{j}X_{2C2}}{X_1X_{3C2}}) \tag{12}$$

Furthermore, according to (4a) and (4b), the input impedance Z_{inCC} of the equivalent circuit shown in Fig. 4(b) is expressed by (13), which is shown at the bottom of this page.

In (13), when

$$X_{2C2}X_{3C1} + (X_{2C1}+X_{2C2})X_{3C2} = 0 \tag{14}$$

the imaginary part of Z_{inCC} [Im(Z_{inCC})] equals zero. It means that the input impedance is purely resistive. And the purely resistive input impedance is expressed as,

$$R_{inCC} = \mathrm{Re}\,(Z_{inCC}) = \frac{1}{R_{ac}}\frac{X_1X_{2C1}X_{3C2}X_4}{X_{2C2}X_{3C1}} = \frac{1}{R_{ac}\,|\mathbf{G}_{CC}|^2} \tag{15}$$

So, ZPA condition is achieved for the equivalent circuit shown in Fig. 4(a) under the conditions of (11) and (14).

Similarly, in order to analyze the CV output characteristic at a ZPA frequency, Fig. 4(a) is modeled as Fig. 4(c), which is essentially a series connected circuit of a reversed L-section matching network and a normal L-section matching network with the parallel impedance X_4. The equivalent variable is expressed as,

$$X_2 = \frac{X_{2V1}X_{2V2}}{X_{2V1}+X_{2V2}} \tag{16}$$

The parallel reactance X_4 does not affect the output voltage, so we only need to analyze the voltage transfer characteristic of the series connected network of the reversed and normal L-section matching networks. According to the analysis of the reversed and normal L-section matching networks in Section II, the resonant condition of the equivalent circuit shown in Fig. 4(c) to achieve CV output is expressed by (17). And the corresponding mathematical model of the constant output voltage $\mathbf{V}_{ab\_CV}$ (or voltage transfer ratio $\mathbf{G}_{CV}$) is given by (18).

$$X_1 + X_{2V1} = X_{2V2} + X_3 = 0 \tag{17}$$

$$\mathbf{V}_{ab\_CV} = \mathrm{j}X_{2V2}\frac{1}{\mathrm{j}X_1}\mathbf{V}_{AB} \times (\text{or } \mathbf{G}_{CV} = \frac{\mathbf{V}_{ab\_CV}}{\mathbf{V}_{AB}} = \frac{\mathrm{j}X_{2V2}}{\mathrm{j}X_1}) \tag{18}$$

Then, under the condition of (17), the input impedance Z_{inCV} of the equivalent circuit shown in Fig. 4(c) is expressed by (19), which is shown at the bottom of this page.

In (19), when

$$(X_{2V1}+X_{2V2})X_4 + X_{2V2}X_3 = 0 \tag{20}$$

the imaginary part of Z_{inCV} [Im(Z_{inCV})] equals zero. It means that the purely resistive input impedance is achieved and

$$\begin{aligned} Z_{inCC} &= \mathrm{Re}\,(Z_{inCC}) + \mathrm{j}\cdot\mathrm{Im}\,(Z_{inCC}) \\ &= \frac{R_{ac}X_1X_4X_{2C1}X_{3C1}X_{2C2}X_{3C2}}{(R_{ac}X_{3C1}X_{2C2})^2 + (X_4\,(X_{2C2}X_{3C1} + (X_{2C1}+X_{2C2})\,X_{3C2}))^2} \\ &\quad + \mathrm{j}\frac{X_1X_{2C1}X_{3C2}X_4^2\,(X_{2C2}X_{3C1} + (X_{2C1}+X_{2C2})\,X_{3C2})}{(R_{ac}X_{3C1}X_{2C2})^2 + (X_4\,(X_{2C2}X_{3C1} + (X_{2C1}+X_{2C2})\,X_{3C2}))^2} \\ Z_{inCV} &= \mathrm{Re}\,(Z_{inCV}) + \mathrm{j}\cdot\mathrm{Im}\,(Z_{inCV}) \\ &= \frac{R_{ac}X_1X_{2V1}X_{2V2}X_3X_4^2}{(X_{2V2}X_3X_4)^2 + (R_{ac}\,((X_{2V1}+X_{2V2})\,X_4 + X_{2V2}X_3))^2} \\ &\quad + \mathrm{j}\frac{R_{ac}^2X_1X_{2V1}X_4\,((X_{2V1}+X_{2V2})\,X_4 + X_{2V2}X_3)}{(X_{2V2}X_3X_4)^2 + (R_{ac}\,((X_{2V1}+X_{2V2})\,X_4 + X_{2V2}X_3))^2} \end{aligned} \tag{13, 19}$$

TABLE III
SUMMARY OF THE ANALYSIS OF THE SIMPLEST RESONANT TUNING CONFIGURATION

The simplest resonant tuning configuration	Fig. 4(a)	
	CC mode with ZPA	CV mode with ZPA
Equivalent circuits	Fig. 4(b)	Fig. 4(c)
Equivalent variables	(10)	(16)
Conditions to achieve load-independent outputs	(11)	(17)
Mathematica models of the constant output current and voltage	(12)	(18)
Conditions to achive load-independent ZPA conditions	(11) and (14)	(17) and (20)
Purely resistive input impedances	(15)	(21)

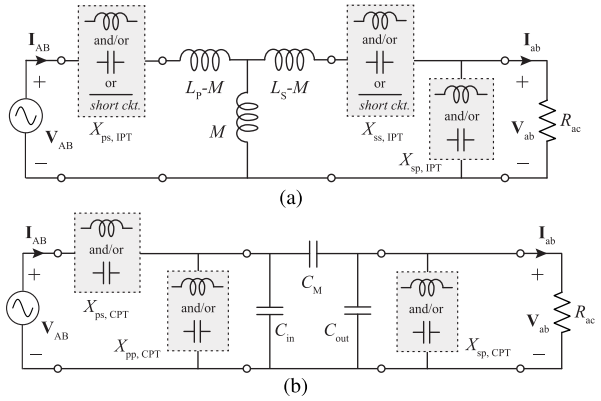

Fig. 5. All the possible compensation topologies in (a) IPT and (b) CPT systems according to Fig. 4(a).

expressed as,

$$R_{\text{inCV}} = \text{Re}(Z_{\text{inCV}}) = R_{\text{ac}}\frac{X_1 X_{2\text{V}1}}{X_{2\text{V}2}X_3} = \frac{R_{\text{ac}}}{|\mathbf{G}_{\text{CV}}|^2} \tag{21}$$

So, the load-independent ZPA condition is achieved for the equivalent circuit shown in Fig. 4(a) under the conditions of (17) and (20).

As aforementioned, the equivalent circuit shown in Fig. 4(a) is the simplest resonant tuning configuration that utilize the minimum number of passive components to achieve CC and CV outputs with ZPA conditions. And a conclusion about the analysis can be made and shown in Tab. III.

IV. APPLICATIONS OF THE PROPOSED SIMPLEST CONFIGURATION IN IPT AND CPT SYSTEMS

According to Fig. 4(a), all the possible compensation topologies in IPT and CPT systems can be analogized, which are shown in Fig. 5(a) and 5(b), respectively. In Fig. 5(a), the loosely coupled transformer consisting of the primary and secondary coils in the IPT system is modeled as its T-model [14], [22]. L_{P} and L_{S} represent the self-inductances of the primary and secondary coils, and M is the mutual inductance between the two coils. The magnetic coupling coefficient k is then determined as $k = M/\sqrt{L_{\text{P}}L_{\text{S}}}$. $X_{\text{ps, IPT}}$, $X_{\text{ss, IPT}}$, and $X_{\text{sp, IPT}}$ are the additional compensation components. Comparing Fig. 5(a) with Fig. 4(a), the series-connected branch $X_{\text{ps, IPT}}$ and $(L_{\text{P}} - M)$, M, the series-connected branch $(L_{\text{S}} - M)$ and $X_{\text{ss, IPT}}$, and $X_{\text{sp, IPT}}$ correspond to X_1, X_2, X_3, and X_4, respectively. For Fig. 5(b), the capacitive coupler in the CPT system is equivalent to its π-model [36], [43], here, C_{in} and C_{out} are the self-capacitances, and C_{M} is the mutual capacitance. $X_{\text{ps, CPT}}$, $X_{\text{pp, CPT}}$, and $X_{\text{sp, CPT}}$ represent the compensation components in the CPT system. Also, comparing Fig. 5(b) with Fig. 4(a), $X_{\text{ps, CPT}}$, the parallel-connected branch $X_{\text{pp, CPT}}$ and C_{in}, C_{M}, and the parallel-connected branch C_{out} and $X_{\text{sp, CPT}}$ correspond to X_1, X_2, X_3, and X_4, respectively.

As shown in Fig. 5(a), $X_{\text{ps, IPT}}$ and $X_{\text{ss, IPT}}$ may be inductive, capacitive, or a short circuit (ckt.), and $X_{\text{sp, IPT}}$ is also either inductive or capacitive. So, there are multiple possible compensation topologies that achieve both CC and CV outputs with ZPA conditions. Among all possible compensation topologies in IPT system, an example shown in Fig. 6(a) is illustrated. The reason for choosing capacitors ($C_{\text{ps, IPT}}$, $C_{\text{ss, IPT}}$, and $C_{\text{sp, IPT}}$) instead of inductors in both the primary and secondary sides is to further improve the system power density and decrease the system loss. Actually, Fig. 6(a) shows an S-SP compensated IPT system. According to the analysis in Section III-B, the equivalent circuits of the S-SP compensation topology that achieve CC output with ZPA and CV output with ZPA are shown in Fig. 6(b) and 6(c) respectively. The detailed analysis are presented in Tab. IV and Tab. V respectively.

V. EVALUATIONS

To verify the above analysis, simulations and experiments are conducted on a 3.3-kW S-SP compensated IPT charging system, as shown in Fig. 7(a). According to Tabs. IV and V, the system design process is shown in Fig. 8, and the calculated parameters are shown in Tab. VI. It can be seen that the designed resonant frequencies for achieving CC output with ZPA and CV output with ZPA are 81.50 kHz and 90.00 kHz, respectively, which are in compliance with SAE J2954 Standard [44]. Based on the system parameters tabulated in Tab. VI, the implemented experimental setup is shown in Fig. 7(b). Symmetrical square-shaped unipolar coils are used for both the primary and the secondary sides. The number of turns and the measured quality factors of the primary and secondary coils are 24 and approximately 500 respectively. And the air gap between the two coils is about 20 cm. EPCOS / TDK B32642B series film capacitors are selected for $C_{\text{ps, IPT}}$, $C_{\text{ss, IPT}}$, and $C_{\text{sp, IPT}}$. In the

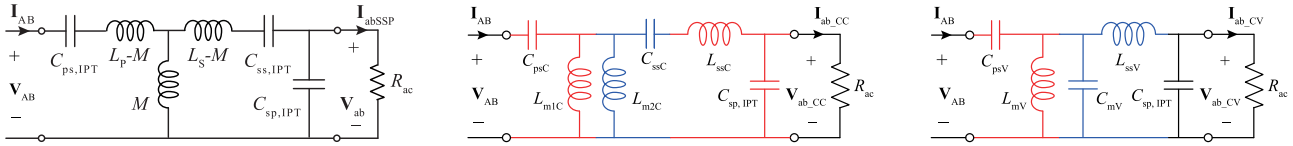

Fig. 6. (a) An example of the simplest IPT compensation topologies: a S-SP compensation topology, (b) the equivalent circuit of the S-SP topology to achieve CC output with ZPA, and (c) the equivalent circuit of the S-SP topology to achieve CV output with ZPA.

TABLE IV

ANALYSIS OF THE S-SP COMPENSATION TOPOLOGY TO ACHIEVE CC OUTPUT WITH ZPA

	CC mode with ZPA	
Equivalent circuits	Fig. 6(b)	
Equivalent variables	$\frac{1}{\mathrm{j}\omega_{cc}C_{psC}} = \frac{1}{\mathrm{j}\omega_{cc}C_{ps,IPT}} + \mathrm{j}\omega_{cc}(L_P - M)$, $\frac{L_{m1C}\cdot L_{m2C}}{L_{m1C}+L_{m2C}} = M$, and $\frac{1}{\mathrm{j}\omega_{cc}C_{ssC}} + \mathrm{j}\omega_{cc}L_{ssC} = \mathrm{j}\omega_{cc}(L_S - M) + \frac{1}{\mathrm{j}\omega_{cc}C_{ss,IPT}}$	(22)
Conditions for achieving load-independent CC output	$\frac{1}{\mathrm{j}\omega_{cc}C_{psC}} + \mathrm{j}\omega_{cc}L_{m1C} = \mathrm{j}\omega_{cc}L_{m2C} + \frac{1}{\mathrm{j}\omega_{cc}C_{ssC}} = \mathrm{j}\omega_{cc}L_{ssC} + \frac{1}{\mathrm{j}\omega_{cc}C_{sp,IPT}} = 0$	(23)
Mathematical models of output current	$\mathbf{I}_{ab\_CC} = \frac{\mathrm{j}\omega_{cc}C_{psC}\cdot\mathrm{j}\omega_{cc}L_{m2C}}{\mathrm{j}\omega_{cc}L_{ssC}}\mathbf{V}_{AB}$ $\left(\text{or } \mathbf{G}_{CC} = \frac{\mathbf{I}_{ab\_CC}}{\mathbf{V}_{AB}} = \frac{\mathrm{j}\omega_{cc}L_{m2C}C_{psC}}{L_{ssC}}\right)$	(24)
Conditions to achieve ZPA	$\begin{cases} \frac{1}{\mathrm{j}\omega_{cc}C_{psC}} + \mathrm{j}\omega_{cc}L_{m1C} = \mathrm{j}\omega_{cc}L_{m2C} + \frac{1}{\mathrm{j}\omega_{cc}C_{ssC}} = \mathrm{j}\omega_{cc}L_{ssC} + \frac{1}{\mathrm{j}\omega_{cc}C_{sp,IPT}} = 0 \\ (\mathrm{j}\omega_{cc}L_{m1C} + \mathrm{j}\omega_{cc}L_{m2C})\,\mathrm{j}\omega_{cc}L_{ssC} + \mathrm{j}\omega_{cc}L_{m2C}\frac{1}{\mathrm{j}\omega_{cc}C_{ssC}} = 0 \end{cases}$	(25)
Purely resistive input impedance	$\mathrm{Re}\,(Z_{inCC}) = \frac{L_{ssC}C_{sp,IPT}}{R_{ac}\omega_{cc}^2 L_{m1C}L_{m2C}C_{psC}C_{ssC}} = \frac{1}{R_{ac}\,\lvert\mathbf{G}_{CC}\rvert^2}$	(26)

TABLE V

ANALYSIS OF THE S-SP COMPENSATION TOPOLOGY TO ACHIEVE CV OUTPUT WITH ZPA

	CV mode with ZPA	
Equivalent circuits	Fig. 6(c)	
Equivalent variables	$\frac{1}{\mathrm{j}\omega_{cv}C_{psV}} = \frac{1}{\mathrm{j}\omega_{cv}C_{ps,IPT}} + \mathrm{j}\omega_{cv}(L_P - M)$, $\mathrm{j}\omega_{cv}L_{mV} \parallel \frac{1}{\mathrm{j}\omega_{cv}C_{mV}} = \mathrm{j}\omega_{cv}M$, and $\mathrm{j}\omega_{cv}L_{ssV} = \mathrm{j}\omega_{cv}(L_S - M) + \frac{1}{\mathrm{j}\omega_{cv}C_{ss,IPT}}$	(27)
Conditions for achieving load-independent CV output	$\frac{1}{\mathrm{j}\omega_{cv}C_{psV}} + \mathrm{j}\omega_{cv}L_{mV} = \frac{1}{\mathrm{j}\omega_{cv}C_{mV}} + \mathrm{j}\omega_{cv}L_{ssV} = 0$	(28)
Mathematical models of output voltage	$\mathbf{V}_{ab\_CV} = \mathrm{j}\omega_{cv}C_{psV}\frac{1}{\mathrm{j}\omega_{cv}C_{mV}}\mathbf{V}_{AB}$ $\left(\text{or } \mathbf{G}_{CV} = \frac{\mathbf{V}_{ab\_CV}}{\mathbf{V}_{AB}} = \frac{C_{psV}}{C_{mV}}\right)$	(29)
Conditions to achieve ZPA	$\begin{cases} \frac{1}{\mathrm{j}\omega_{cv}C_{psV}} + \mathrm{j}\omega_{cv}L_{mV} = \frac{1}{\mathrm{j}\omega_{cv}C_{mV}} + \mathrm{j}\omega_{cv}L_{ssV} = 0 \\ \left(\mathrm{j}\omega_{cv}L_{mV} + \frac{1}{\mathrm{j}\omega_{cv}C_{mV}}\right)\frac{1}{\mathrm{j}\omega_{cc}C_{sp,IPT}} + \frac{1}{\mathrm{j}\omega_{cv}C_{mV}}\mathrm{j}\omega_{cv}L_{ssV} = 0 \end{cases}$	(30)
Purely resistive input impedance	$\mathrm{Re}\,(Z_{inCV}) = \frac{R_{ac}L_{ssV}C_{mV}}{L_{mV}C_{psV}} = \frac{R_{ac}}{\lvert\mathbf{G}_{CV}\rvert^2}$	(31)

experimental prototype, the capacitor bank is designed by connecting combinations of multiple standard capacitors in series and parallel, which can make the difference between the experimental value and the theoretical value less than 0.2 nF and increase the withstand voltage of the capacitor bank. Silicon Carbide (SiC) MOSFETs C2M0080120D are used to implement the input single phase full-bridge inverter. Also, SiC diodes IDW30G65C are adopted at the secondary side single phase full-wave bridge rectifier. The diode rectifier with LC filter is used to rectify the AC output current of the S-SP compensation topology before connecting to the battery. The rectifier output LC filter is designed to be 680 μH and 220 nF. A Chroma 62100H programmable DC power supply is used to drive the IPT system. Also, a Chroma DC Electronic Load 63210 is used to emulate the battery.

Fig. 9 shows the simulation results of the transconductance, voltage transfer ratio, and input phase angle of the S-SP compensation topology versus frequency at different load conditions. It can be seen that the load-independent transconductance of 0.04845 and the load-independent ZPA are achieved at 81.5 kHz simultaneously. Additionally, the load-independent CV output with ZPA is realized at 90.0 kHz.

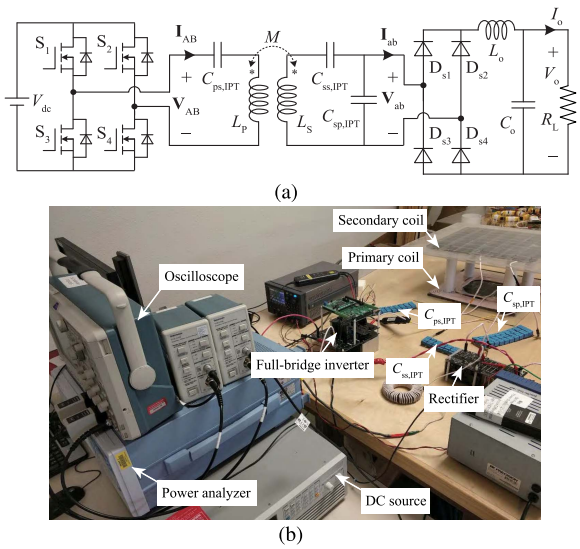

Fig. 7. (a) The S-SP compensated IPT system and (b) the experiment setup.

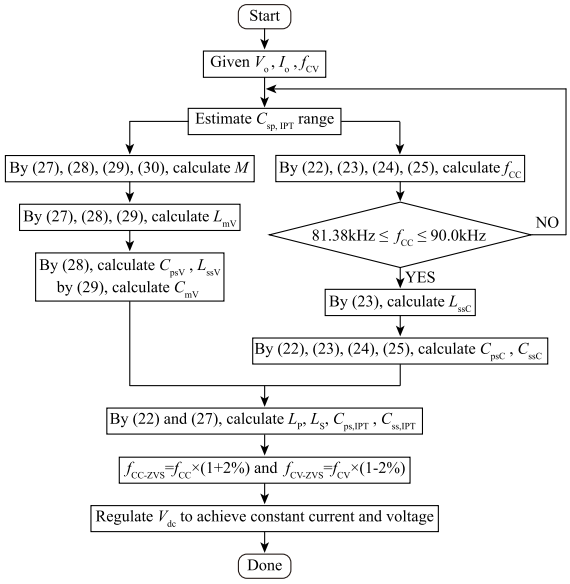

Fig. 8. System design process.

TABLE VI

PARAMETERS OF THE S-SP COMPENSATED IPT SYSTEM

Parameters	Value (Unit)	Parameters	Value (Unit)
L_P	288.00 μH	$C_{ps,IPT}$	12.17 nF
L_S	288.00 μH	$C_{ss,IPT}$	13.25 nF
k	0.14	$C_{sp,IPT}$	60.00 nF
f_{cc}	81.50 kHz	f_{cv}	90.00 kHz

When the S-SP compensated IPT prototype operates at 81.5 kHz and 90.0 kHz, respectively, the measured waveforms of the input voltage $v_{AB}(t)$, input current $i_{AB}(t)$, output DC voltage $v_o(t)$, and output DC current $i_o(t)$ are shown in Fig. 10(a) and 10(b). From Fig. 10(a) and 10(b), the input currents are nearly in phase with the input voltage, which mean that ZPA conditions are achieved in both CC and CV modes and verify the theoretic analysis and simulation results shown in Fig. 9.

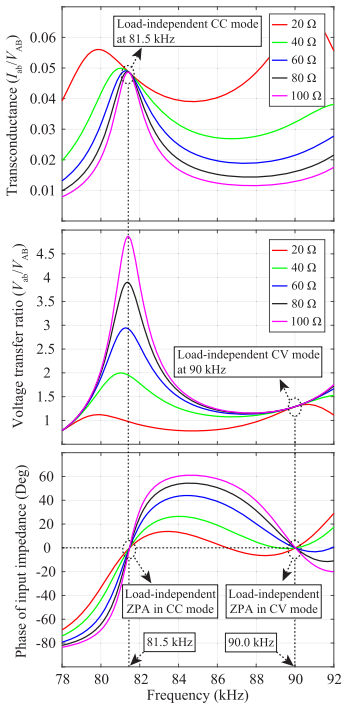

Fig. 9. Simulated transconductance, voltage transfer ratio, and phase angle of the input impedance of the S-SP compensation topology.

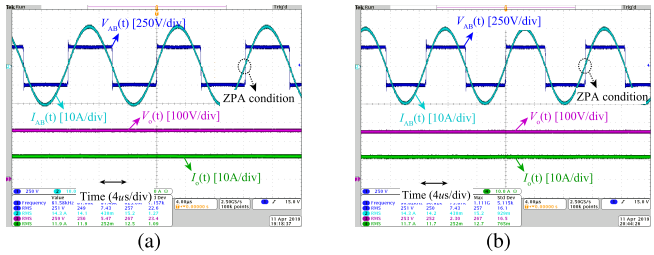

Fig. 10. Waveforms of $v_{AB}(t)$, $i_{AB}(t)$, $v_o(t)$, and $i_o(t)$ when the IPT system operates at (a) 81.5 kHz and (b) 90.0 kHz.

Under the condition of ZPA operation, the method that slightly changes the value of a compensation component [9], [12], [13] or the system operating frequency [8], [14] has been proposed to ensure ZVS for the primary MOSFET-based inverter to reduce its switching loss. In this paper, the method of changing the operating frequency is adopted. Specifically, the operating frequency is changed from 81.5 kHz to 83 kHz in CC mode. In CV mode, 88 kHz is adopted. In this case, however, the voltage and current transfer characteristics will depend on the variation of the load from Fig. 9. In addition, the output characteristics are inevitably affected by the components parasitic resistance [8], [9] and some uncertain factors [30], for example, the manufacturing tolerance. Thereby, a feedback control is necessary to achieve constant output current in CC mode and constant output voltage in CV mode. Many feedback control methods have been proposed, for example, regulating the input voltage, changing the operating frequency [8], and using the fix frequency duty cycle control for the inverter [9]. In this paper, the method of slightly regulating V_{dc} is adopted because it does not affect the ZVS over the full range of charging profile. The measured $i_o(t)$ and $v_o(t)$

TABLE VII
COMPARISON OF THE PUBLICATIONS FOR CC OUTPUT WITH ZPA AND CV OUTPUT WITH ZPA

Reference		P_{out}	f_{CC} and f_{CV}	η_{CC} and η_{CV}	I_{CC} and V_{CV}	Limitation
This paper		3.3 kW	$f_{CC} = 81.5$ kHz $f_{CV} = 90.0$ kHz	$\eta_{CC} = 93.6\%$ $\eta_{CV} = 94.1\%$	$I_{CC} = 12.22$ A $V_{CV} = 270$ V	Additional power semiconductor devices
Hybrid topology	[21]	15 W	$f_{CC} = f_{CV} = 200$ kHz	$\eta_{CC} = 92.5\%$ $\eta_{CV} = 93.7\%$	$I_{CC} = 1$ A $V_{CV} = 15$ V	
	[39]	192 W	$f_{CC} = f_{CV} = 500$ kHz	$\eta_{CC} = 92.8\%$ $\eta_{CV} = 92.4\%$	$I_{CC} = 2$ A $V_{CV} = 96$ V	
	[40]	216 W	$f_{CC} = f_{CV} = 500$ kHz	$\eta_{CC} = 89.5\%$ $\eta_{CV} = 91.9\%$	$I_{CC} = 3$ A $V_{CV} = 72$ V	
Double-sided LCC topology	[8]	6.6 kW	$f_{CC} = 68$ kHz $f_{CV} = 79.1$ kHz	$\eta_{CC} = 96.1\%$ $\eta_{CV} = 95.1\%$	$I_{CC} = 15.7$ A $V_{CV} = 420$ V	Low power density
	[9]	24 W	$f_{CC} = 206.6$ kHz $f_{CV} = 259.9$ kHz	$\eta_{CC} = 93.7\%$ $\eta_{CV} = 91.8\%$	$I_{CC} = 1$ A $V_{CV} = 24$ V	

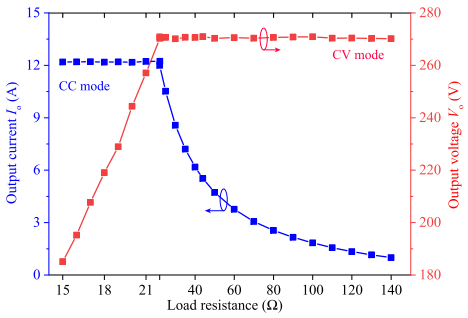

Fig. 11. Measured output current and voltage of the S-SP compensated IPT system versus the load resistance.

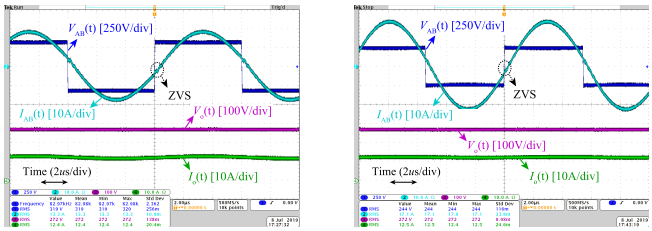

(a) (b)

Fig. 12. Waveforms of $v_{AB}(t)$, $i_{AB}(t)$, $v_o(t)$, and $i_o(t)$ in (a) CC and (b) mode at 3.3-kW output power.

are shown in Fig. 11. The system operates at 83.0 kHz when the load resistance is continuously changed from 15 Ω to 22 Ω (full load), while the system operates at 88 kHz when the load varies from 22 Ω to 140 Ω. It can be seen that CC/CV charging profile is achieved. Furthermore, Figs. 12(a) and 12(b) show the measured waveforms of $v_{AB}(t)$, $i_{AB}(t)$, $v_o(t)$ and $i_o(t)$ at 3.3-kW output power in CC and CV charging modes respectively. Fig. 13 shows the measured $v_{AB}(t)$, $i_{AB}(t)$, $v_o(t)$, and $i_o(t)$ at 1.65-kW output power. From Figs. 12 and 13, the input currents slightly lag the input voltage in both CC and CV modes, which means that the ZVS operations are achieved.

Figs. 14(a) and 14(b) shows the measured efficiencies, η_{CC} and η_{CV}, of the S-SP compensated IPT system from the DC input of the inverter to the load at 3.3-kW output power. The peak efficiencies in CC and CV mode are shown

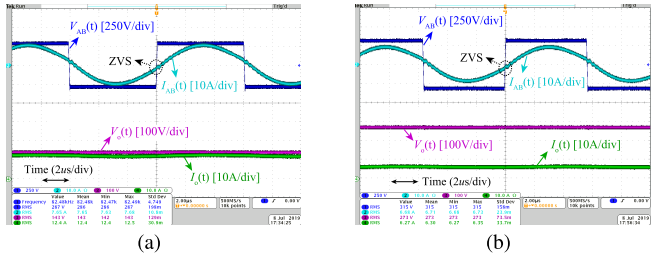

(a) (b)

Fig. 13. Waveforms of $v_{AB}(t)$, $i_{AB}(t)$, $v_o(t)$, and $i_o(t)$ in (a) CC and (b) mode at half power.

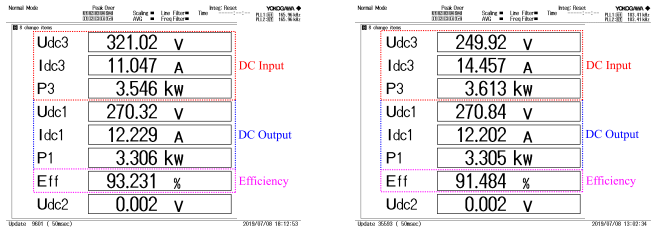

(a) (b)

Fig. 14. Screen capture of the IPT system efficiency measurement in (a) CC and (b) CV modes at 3.3-kW output power.

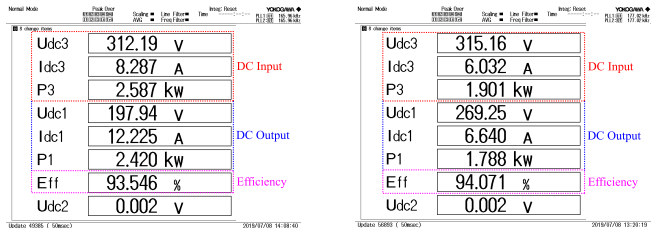

(a) (b)

Fig. 15. Screen capture of the peak efficiency measurement in (a) CC and (b) CV modes.

in Figs. 15(a) and 15(b). In CC mode, the efficiency at full power and the peak efficiency are up to 93.2% and 93.6%, respectively. Besides, the peak efficiency in CV mode is 94.1%.

The performances of the proposed IPT system in this paper are compared with the previous works, as given in Tab VII.

The designed IPT system can achieve CC output with ZPA and CV output with ZPA using the minimum number of compensation components and has competitive efficiencies in both CC and CV modes. Furthermore, the uneconomical power semiconductor devices for switching topologies and the compensation inductors that take up large volume, weight, and loss are omitted.

VI. Conclusion

In order to improve the power density and efficiency and reduce the cost of the wireless battery charging system, in this paper, the simplest resonant circuit configuration with minimal passive component counts is proposed to realize CC and CV outputs at two different ZPA frequencies. According to the proposed configuration, all the possible IPT and CPT topologies are derived. The main benefit for these IPT and CPT topologies is that CC and CV outputs with ZPA operations can be achieved by using the minimum number of additional compensation components. A 3.3-kW S-SP compensated IPT system is analyzed and implemented to verify CC and CV outputs at ZPA frequencies. In addition, a design method is proposed for the S-SP topology to make the system operating frequencies in both CC and CV modes meet the standard requirements of SAE J2954.

References

[1] Z. Zhang, H. Pang, A. Georgiadis, and C. Cecati, "Wireless power transfer—An overview," *IEEE Trans. Ind. Electron.*, vol. 66, no. 2, pp. 1044–1058, Feb. 2019.

[2] S. Li and C. C. Mi, "Wireless power transfer for electric vehicle applications," *IEEE J. Emerg. Sel. Topics Power Electron.*, vol. 3, no. 1, pp. 4–17, Mar. 2015.

[3] H. Tu, H. Feng, S. Srdic, and S. Lukic, "Extreme fast charging of electric vehicles: A technology overview," *IEEE Trans. Transport. Electrific.*, vol. 5, no. 4, pp. 861–878, Dec. 2019.

[4] A. Ahmad, M. S. Alam, and R. Chabaan, "A comprehensive review of wireless charging technologies for electric vehicles," *IEEE Trans. Transport. Electrific.*, vol. 4, no. 1, pp. 38–63, Mar. 2018.

[5] G. Buja, M. Bertoluzzo, and K. N. Mude, "Design and experimentation of WPT charger for electric city car," *IEEE Trans. Ind. Electron.*, vol. 62, no. 12, pp. 7436–7447, Dec. 2015.

[6] D. H. Tran, V. B. Vu, and W. Choi, "Design of a high-efficiency wireless power transfer system with intermediate coils for the on-board chargers of electric vehicles," *IEEE Trans. Power Electron.*, vol. 33, no. 1, pp. 175–187, Jan. 2018.

[7] C. Zheng *et al.*, "High-efficiency contactless power transfer system for electric vehicle battery charging application," *IEEE J. Emerg. Sel. Topics Power Electron.*, vol. 3, no. 1, pp. 65–74, Mar. 2015.

[8] V.-B. Vu, D.-H. Tran, and W. Choi, "Implementation of the constant current and constant voltage charge of inductive power transfer systems with the double-sided LCC compensation topology for electric vehicle battery charge applications," *IEEE Trans. Power Electron.*, vol. 33, no. 9, pp. 7398–7410, Sep. 2018.

[9] X. Qu, H. Chu, S.-C. Wong, and C. K. Tse, "An IPT battery charger with near unity power factor and load-independent constant output combating design constraints of input voltage and transformer parameters," *IEEE Trans. Power Electron.*, vol. 34, no. 8, pp. 7719–7727, Aug. 2019.

[10] S. Samanta and A. K. Rathore, "Analysis and design of load-independent ZPA operation for P/S, PS/S, P/SP, and PS/SP tank networks in IPT applications," *IEEE Trans. Power Electron.*, vol. 33, no. 8, pp. 6476–6482, Aug. 2018.

[11] M. Kim, D.-M. Joo, and B. K. Lee, "Design and control of inductive power transfer system for electric vehicles considering wide variation of output voltage and coupling coefficient," *IEEE Trans. Power Electron.*, vol. 34, no. 2, pp. 1197–1208, Feb. 2019.

[12] S. Li, W. Li, J. Deng, T. D. Nguyen, and C. C. Mi, "A double-sided LCC compensation network and its tuning method for wireless power transfer," *IEEE Trans. Veh. Technol.*, vol. 64, no. 6, pp. 2261–2273, Jun. 2015.

[13] Y. Wang *et al.*, "A double-T-type compensation network and its tuning method for IPT system," *IEEE Trans. Ind. Appl.*, vol. 53, no. 5, pp. 4757–4767, Sep. 2017.

[14] Y. H. Sohn, B. H. Choi, E. S. Lee, G. C. Lim, G.-H. Cho, and C. T. Rim, "General unified analyses of two-capacitor inductive power transfer systems: Equivalence of current-source SS and SP compensations," *IEEE Trans. Power Electron.*, vol. 30, no. 11, pp. 6030–6045, Nov. 2015.

[15] X. Zhang *et al.*, "A control strategy for efficiency optimization and wide ZVS operation range in bidirectional inductive power transfer system," *IEEE Trans. Ind. Electron.*, vol. 66, no. 8, pp. 5958–5969, Aug. 2019.

[16] H. H. Wu, A. Gilchrist, K. D. Sealy, and D. Bronson, "A high efficiency 5 kW inductive charger for EVs using dual side control," *IEEE Trans. Ind. Informat.*, vol. 8, no. 3, pp. 585–595, Aug. 2012.

[17] C.-S. Wang, O. H. Stielau, and G. A. Covic, "Design considerations for a contactless electric vehicle battery charger," *IEEE Trans. Ind. Electron.*, vol. 52, no. 5, pp. 1308–1314, Oct. 2005.

[18] C.-S. Wang, G. A. Covic, and O. H. Stielau, "Power transfer capability and bifurcation phenomena of loosely coupled inductive power transfer systems," *IEEE Trans. Ind. Electron.*, vol. 51, no. 1, pp. 148–157, Feb. 2004.

[19] W. Zhang, S.-C. Wong, C. K. Tse, and Q. Chen, "Load-independent duality of current and voltage outputs of a Series- or parallel-compensated inductive power transfer converter with optimized efficiency," *IEEE J. Emerg. Sel. Topics Power Electron.*, vol. 3, no. 1, pp. 137–146, Mar. 2015.

[20] X. Qu, W. Zhang, S.-C. Wong, and C. K. Tse, "Design of a current-source-output inductive power transfer LED lighting system," *IEEE J. Emerg. Sel. Topics Power Electron.*, vol. 3, no. 1, pp. 306–314, Mar. 2015.

[21] X. Qu, H. Han, S.-C. Wong, C. K. Tse, and W. Chen, "Hybrid IPT topologies with constant current or constant voltage output for battery charging applications," *IEEE Trans. Power Electron.*, vol. 30, no. 11, pp. 6329–6337, Nov. 2015.

[22] Y.-H. Sohn, B. Choi, G.-H. Cho, and C. Rim, "Gyrator-based analysis of resonant circuits in inductive power transfer systems," *IEEE Trans. Power Electron.*, vol. 31, no. 10, pp. 6824–6843, Oct. 2016.

[23] W. Zhang and C. C. Mi, "Compensation topologies of high-power wireless power transfer systems," *IEEE Trans. Veh. Technol.*, vol. 65, no. 6, pp. 4768–4778, Jun. 2016.

[24] Z. Huang, S.-C. Wong, and C. K. Tse, "Design of a single-stage Inductive-Power-Transfer converter for efficient EV battery charging," *IEEE Trans. Veh. Technol.*, vol. 66, no. 7, pp. 5808–5821, Jul. 2017.

[25] J. Hou, Q. Chen, Z. Zhang, S.-C. Wong, and C. K. Tse, "Analysis of output current characteristics for higher order primary compensation in inductive power transfer systems," *IEEE Trans. Power Electron.*, vol. 33, no. 8, pp. 6807–6821, Aug. 2018.

[26] Z. Huang, S.-C. Wong, and C. K. Tse, "An inductive-power-transfer converter with high efficiency throughout battery-charging process," *IEEE Trans. Power Electron.*, vol. 34, no. 10, pp. 10245–10255, Oct. 2019.

[27] J. Lu, G. Zhu, D. Lin, S.-C. Wong, and J. Jiang, "Load-independent voltage and current transfer characteristics of high-order resonant network in IPT system," *IEEE J. Emerg. Sel. Topics Power Electron.*, vol. 7, no. 1, pp. 422–436, Mar. 2019.

[28] W. Zhang, S.-C. Wong, C. K. Tse, and Q. Chen, "Analysis and comparison of secondary series- and parallel-compensated inductive power transfer systems operating for optimal efficiency and load-independent voltage-transfer ratio," *IEEE Trans. Power Electron.*, vol. 29, no. 6, pp. 2979–2990, Jun. 2014.

[29] W. Zhang, S.-C. Wong, C. K. Tse, and Q. Chen, "Design for efficiency optimization and voltage controllability of series–series compensated inductive power transfer systems," *IEEE Trans. Power Electron.*, vol. 29, no. 1, pp. 191–200, Jan. 2014.

[30] J. Lu, G. Zhu, H. Wang, F. Lu, J. Jiang, and C. C. Mi, "Sensitivity analysis of inductive power transfer systems with voltage-fed compensation topologies," *IEEE Trans. Veh. Technol.*, vol. 68, no. 5, pp. 4502–4513, May 2019.

[31] J. Hou, Q. Chen, S.-C. Wong, C. K. Tse, and X. Ruan, "Analysis and control of series/series-parallel compensated resonant converter for contactless power transfer," *IEEE J. Emerg. Sel. Topics Power Electron.*, vol. 3, no. 1, pp. 124–136, Mar. 2015.

[32] J. Hou, Q. Chen, X. Ren, X. Ruan, S.-C. Wong, and C. K. Tse, "Precise characteristics analysis of Series/Series-parallel compensated contactless resonant converter," *IEEE J. Emerg. Sel. Topics Power Electron.*, vol. 3, no. 1, pp. 101–110, Mar. 2015.
[33] Y. Yao, Y. Wang, X. Liu, K. Lu, and D. Xu, "Analysis and design of an S/SP compensated IPT system to minimize output voltage fluctuation versus coupling coefficient and load variation," *IEEE Trans. Veh. Technol.*, vol. 67, no. 10, pp. 9262–9272, Oct. 2018.
[34] X. Qu, Y. Jing, H. Han, S.-C. Wong, and C. K. Tse, "Higher order compensation for inductive-power-transfer converters with constant-voltage or constant-current output combating transformer parameter constraints," *IEEE Trans. Power Electron.*, vol. 32, no. 1, pp. 394–405, Jan. 2017.
[35] X. Qu *et al.*, "Wide design range of constant output current using double-sided LC compensation circuits for inductive-power-transfer applications," *IEEE Trans. Power Electron.*, vol. 34, no. 3, pp. 2364–2374, Mar. 2019.
[36] H. Zhang, F. Lu, H. Hofmann, W. Liu, and C. C. Mi, "A four-plate compact capacitive coupler design and LCL-compensated topology for capacitive power transfer in electric vehicle charging application," *IEEE Trans. Power Electron.*, vol. 31, no. 12, pp. 8541–8551, Dec. 2016.
[37] Y.-G. Su, S.-Y. Xie, A. P. Hu, C.-S. Tang, W. Zhou, and L. Huang, "Capacitive power transfer system with a mixed-resonant topology for constant-current multiple-pickup applications," *IEEE Trans. Power Electron.*, vol. 32, no. 11, pp. 8778–8786, Nov. 2017.
[38] F. Lu, H. Zhang, H. Hofmann, and C. C. Mi, "A double-sided LC-compensation circuit for loosely coupled capacitive power transfer," *IEEE Trans. Power Electron.*, vol. 33, no. 2, pp. 1633–1643, Feb. 2018.
[39] R. Mai, Y. Chen, Y. Li, Y. Zhang, G. Cao, and Z. He, "Inductive power transfer for massive electric bicycles charging based on hybrid topology switching with a single inverter," *IEEE Trans. Power Electron.*, vol. 32, no. 8, pp. 5897–5906, Aug. 2017.
[40] Y. Chen, Z. Kou, Y. Zhang, Z. He, R. Mai, and G. Cao, "Hybrid topology with configurable charge current and charge voltage output-based WPT charger for massive electric bicycles," *IEEE J. Emerg. Sel. Topics Power Electron.*, vol. 6, no. 3, pp. 1581–1594, Sep. 2018.
[41] A. Kumar, S. Sinha, A. Sepahvand, and K. K. Afridi, "Improved design optimization for high-efficiency matching networks," *IEEE Trans. Power Electron.*, vol. 33, no. 1, pp. 37–50, Jan. 2018.
[42] Y. Han and D. J. Perreault, "Analysis and design of high efficiency matching networks," *IEEE Trans. Power Electron.*, vol. 21, no. 5, pp. 1484–1491, Sep. 2006.
[43] S. Li, Z. Liu, H. Zhao, L. Zhu, C. Shuai, and Z. Chen, "Wireless power transfer by electric field resonance and its application in dynamic charging," *IEEE Trans. Ind. Electron.*, vol. 63, no. 10, pp. 6602–6612, Oct. 2016.
[44] J. Schneider, "Wireless power transfer for light-duty plug-in/electric vehicles and alignment methodology," SAE Tech. Rep. J2954, Nov. 2017.

Jianghua Lu (Student Member, IEEE) was born in Hubei, China, in 1989. He received the M.S. degree from the Wuhan University of Technology, in 2016. He is currently pursuing the joint Ph.D. degree in electrical engineering with the Wuhan University of Technology and the Department of Electrical and Computer Engineering, San Diego State University, San Diego, CA, USA.

In 2018, he received the funding from the China Scholarship Council. His current research interests include wireless power transfer and resonant converters.

Guorong Zhu (Senior Member, IEEE) received the Ph.D. degree in electrical engineering from the Huazhong University of Science and Technology, Wuhan, China, in 2009.

From 2002 to 2005, she was a Lecturer with the School of Electrical Engineering, Wuhan University of Science and Technology, Wuhan. From 2009 to 2011, she was a Research Assistant/Research Associate with the Department of Electronics and Information Engineering, The Hong Kong Polytechnic University, Hong Kong. She is currently an Associate Professor with the School of Automation, Wuhan University of Technology, Wuhan. Her main research interests are focused on wireless power transfer and the reliability of power electronics systems.

Deyan Lin (Member, IEEE) received the B.Sc. and M.A.Sc. degrees in electrical engineering from the Huazhong University of Science and Technology, Wuhan, China, in 1995 and 2004, respectively, and the Ph.D. degree from the City University of Hong Kong, Hong Kong, in 2012.

From 1995 to 1999, he was a Teaching Assistant with the Department of Electrical Engineering, Jianghan University, Wuhan, where he became a Lecturer in 1999. From 2008 to 2009, he was a Senior Research Assistant at the City University of Hong Kong. He is currently a Professor with the School of Automation, Wuhan University of Technology, Wuhan, and a Post-Doctoral Fellow of the Department of Electrical and Electronics Engineering, The University of Hong Kong, Hong Kong. His research interests include wireless power transfer, memristors, modeling, and the control of gas-discharge lamps and light-emitting diode technology.

Yiming Zhang (Member, IEEE) received the B.S. and Ph.D. degrees in electrical engineering from Tsinghua University, Beijing, China, in 2011 and 2016, respectively.

He is currently a Post-Doctoral Researcher with San Diego State University, San Diego, CA, USA. His research interests include wireless power transfer for electric vehicles and mobile phones, and resonant converters.

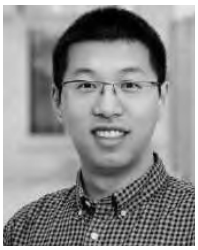

Haoran Wang (Member, IEEE) received the B.S. and M.S. degrees in control science and engineering from the Wuhan University of Technology, Wuhan, China, in 2012 and 2015, respectively, and the Ph.D. degree in power electronics from the Center of Reliable Power Electronics (CORPE), Aalborg University, Aalborg, Denmark, in 2018.

From July 2013 to September 2014, he was a Research Assistant with the Department of Electrical Engineering, Tsinghua University, Beijing, China. He was a Visiting Scientist with ETH Zurich, Switzerland, from December 2017 to April 2018. He is currently an Assistant Professor with Aalborg University. His research interests include capacitors in power electronics, the reliability of power electronics systems, and the multiobjective life-cycle performance optimization of power electronics systems.

Chunting Chris Mi (Fellow, IEEE) received the B.S.E.E. and M.S.E.E. degrees in electrical engineering from Northwestern Polytechnical University, Xi'an, China, in 1985 and 1988, respectively, and the Ph.D. degree in electrical engineering from the University of Toronto, Toronto, ON, Canada, in 2001.

He is a Professor and the Chair of electrical and computer engineering and the Director of the Department of Energy (DOE), funded by the Graduate Automotive Technology Education (GATE) Center for Electric Drive Transportation, San Diego State University, San Diego, USA. Prior to joining SDSU, he was with the University of Michigan, Dearborn, from 2001 to 2015.